

Li-ion Capacitor via Solvent-Co-Intercalation Process from Spent Li-ion Batteries

Madhusoodhanan Lathika Divya,^[a] Yun-Sung Lee,^{*[b]} and Vanchiappan Aravindan^{*[a]}

Li-intercalation into graphite is the key underlying mechanism in the energy storage process. However, the intercalation of solvated Li-ion/co-intercalation of Li-ion into graphite is considered unfitting, as it can initiate exfoliation of graphene layers. But later, it is revealed that co-intercalation of Li does not destroy graphene layers and the compatibility of graphite host; moreover, the type of lithiated solvent molecule decides the reversibility of co-intercalation process. Here, we report the fabrication of glyme-based Li-ion capacitors (LIC). The battery-type electrode, graphite, is recovered from a spent Li-ion battery (LIB) and serves as an anode, active along with a

commercial activated carbon cathode. The assembled LIC with a co-intercalation mechanism could deliver a maximum energy density of $\sim 46.40 \text{ Wh kg}^{-1}$ at ambient temperature conditions. In addition, the performance of LIC is studied at various temperature conditions to ensure compatibility at different environmental conditions. The developed dual-carbon LICs with low cost and high performance using recovered graphite as the anode can be considered as a real solution for recycling spent LIBs in an effective way by incorporating the waste-to-wealth approach.

1. Introduction

Energy storage systems are expected to gain progressively more cheering in the years ahead due to the rising demand for unceasing electricity supply and mounting interest in renewable energy power generation.^[1] Electrochemical energy storage devices (EES) transformed the energy sector of the 21st century and are fetching more attention for dropping fossil fuel consumption in transportation and also to balance the electric grid. Li-ion capacitor (LIC) or hybrid ion capacitor is an effective combination of both battery and supercapacitor technology, which combines the best features of electric double-layer capacitors (EDLCs) and Li-ion batteries (LIBs).^[2–8] LICs generally consist of one electrostatic (capacitive) and one electrochemical (battery) electrodes. They can exhibit higher energy density than an EDLC and more durability than a LIB, without self-discharge and thermal runaway conditions.^[9–11] LICs with dual carbon electrodes are a promising option as they are of low cost, environment-friendly, and can ensure adequate safety.^[12–15] Dual carbon LICs use high-capacity carbonaceous materials like graphite, hard carbon, or soft carbon with Li^+ ion insertion active sites as a battery type electrode and EDLC type

carbon material as a positive electrode.^[13,15–17] Long-range ordered graphite plays a vital role as the anode active material in dual-carbon LICs because of its low de-/lithiation potential ($\sim 0.1 \text{ V}$ vs. Li) and a high theoretical capacity of $\sim 372 \text{ mAh g}^{-1}$.^[18–19] Electrochemical lithiation in graphite anode is a staging phenomenon that leads to the formation of Li_xC_6 ($x=1$).^[20–21] Dual-carbon LICs with a pre-lithiated graphitic anode and activated carbon (AC) cathode have been marketed successfully. Global LIC market size is estimated to reach USD 27 million by 2026 from USD 20 million in 2020.^[22] However, graphite usage in LIBs and LICs are mainly targeted for electric vehicles, consumer electronics, and other energy storage applications, which is expected to surge the graphite demand in the upcoming years. Moreover, the supply of natural graphite is limited, and hence the price of graphite is anticipated to rise during the forthcoming years.^[23] It is also important to develop technology that guarantees a resource-efficient and economically reasonable LIB recycling system to assure the future supply of material components and ensure environmental safety. Reuse of graphite flakes recovered from spent batteries is a potential solution to meet the future demands of graphite.^[23–25] In this line, we have already explored the possibility of using recovered graphite (RG) from spent LIB as an anode active material in the graphite-based battery,^[26–27] hybrid capacitor devices,^[15,28] and synthesis of graphene.^[29] Dual carbon LIC fabricated with pre-lithiated graphite from spent LIB as an anode, and AC cathode could store maximum energy of $185.54 \text{ Wh kg}^{-1}$ in ambient conditions in conventional carbonate solutions.^[15]

The chemistry of the co-intercalation process differs from the conventional Li-ion intercalation mechanism in graphite, in which solvated Li-ions are de-solvated before intercalation, and only the bare ions are getting inserted. However, in co-intercalation, the desolvation step is absent and hence exhibits minimized interaction between solvated Li-ions and graphene

[a] M. L. Divya, Dr. V. Aravindan
Department of Chemistry
Indian Institute of Science Education and Research (IISER)
Tirupati 517507, India
E-mail: aravind_van@yahoo.com

[b] Prof. Y.-S. Lee
Faculty of Applied Chemical Engineering
Chonnam National University
Gwangju - 500 757, Republic of Korea
E-mail: leeys@chonnam.ac.kr

 Supporting information for this article is available on the WWW under
<https://doi.org/10.1002/batt.202000316>

 An invited contribution to a Special Collection dedicated to Metal-Ion Hybrid Supercapacitors

layers, which outcomes rapid diffusion kinetics. Moreover, the marginal growth of the solid electrolyte interphase (SEI) layer on the graphite surface ensures easy transport of solvated Li-ions between the graphene layers. In the development of LIB technology, co-intercalation of solvated Li-ions into graphite was considered unsuitable as it can cause rapid cell death because of gas evolution and exfoliation of graphene layers. The first reversible co-intercalation of solvated Li-ions into graphite was reported by Abe *et al.*^[30] The electrochemical behavior of intercalation of solvated Li-ion differs from that of bare Li-ion with disparities in the value of specific capacity and intercalation potential. The co-intercalation product, graphite intercalation compounds (GICs), are highly stable due to the absence of direct interaction between graphene layers and intercalated ions. This extra stability leads to a higher co-intercalation potential between 0.5–1.0 V vs. Li and is much higher than ~0.15 V vs. Li of traditional Li-ion intercalation into graphite. Moreover, the involvement of solvent molecule in the intercalant weight restricts the available space for alkali ions, and hence there is a decrease in the capacity value in co-intercalation. However, the absence of desolvation at the electrode surface, which is the rate-determining step in the charge transfer reaction, and the limited growth of the SEI layer contribute to an enhanced reaction rate. Simulation studies have shown that the intense solvation energy of ion-solvent complexes and high LUMO level of intercalant is vital for co-intercalation phenomena.^[31–32] The LUMO level of solvent should be higher than the Fermi level of graphite. Recently, Park *et al.*^[31] reviewed the developments made in understanding the co-intercalation mechanism in graphite with various environments. The real chemistry behind this solvated ion intercalation mechanism is not fully understood. Further studies are necessary to understand the configuration of solvated ion, electrolyte systems, and charge transfer mechanism in detail.

Herein, we studied the phenomenon of co-intercalation of solvated Li-ions into graphite material recycled from spent LIB by using Lithium hexafluorophosphate (LiPF_6) in a non-flammable solvent tetraethylene glycol dimethyl ether (TEGDME) as the electrolyte. We also report the electrochemical performance of a co-intercalation-based LIC fabricated with pre-lithiated graphite (*p*-RG) anode and AC cathode. RG serves as a battery type electrode to host glyme-solvated Li^+ ions, and AC acts as a capacitor type electrode *via* adsorption-desorption of anions on its surface. We also related the performance of this new type of glyme-based LIC, which works by the co-intercalation mechanism with the previously reported RG/AC system based on the conventional intercalation process.

2. Results and Discussion

The crystal structure and the phase composition of the RG material were analyzed through powder X-ray diffraction (XRD, Figure 1a and Figure S1). The observed diffraction peaks match well with the literature Joint Committee on Powder Diffraction Standards (JCPDS) 01-075-1621. The diffraction peaks position along with a prominent sharp peak at 26.22° corresponding to

(002) crystallographic plane of hexagonal graphite with a space group of $P6_3mc$. The other peaks positioned at 42.2° , 44.3° , 53.9° , 59.4° and 77.2° agreed to the planes (100), (101), (004), (103) and (110), respectively. The presence of a sharp diffraction peak corresponding to the interplanar spacing of 3.395 \AA and the absence of extra peaks indicates the purity of the RG sample recovered from spent LIB. The structural changes in the RG were analyzed by Raman spectrum (Figure 1b), which shows three prominent peaks corresponding to D band ($\sim 1355\text{ cm}^{-1}$), G band ($\sim 1585\text{ cm}^{-1}$), and 2D band ($\sim 2713\text{ cm}^{-1}$). The G band refers to in-plane vibrations of sp^2 carbon atoms, and the D band is due to out of plane vibrations of disordered graphite, representing structural defects. The peak intensity ratio corresponding to the D and G band (I_D/I_G) was obtained as 0.42, indicating fewer structural defects. The 2D band between $2500 - 2800\text{ cm}^{-1}$ represents second order two phonon processes and is in combination with the G band is the Raman signature of graphitic sp^2 materials. The surface chemistry or elemental composition on the surface of the RG was analyzed by X-ray photoelectron spectroscopy (XPS). The position and intensity of peaks on the survey scan represent the surface functional groups. The raw XPS spectrum (Figure S2) shows peaks corresponding to C and O functionalities. A high-resolution scan of the elemental peaks corresponds to different states of the element with slightly different binding energies. The C1s spectrum can be deconvoluted into three peaks corresponding to contributions from three different functional groups (Figure 1c). The peak at $\sim 284.6\text{ eV}$ indicates non-oxidized alkaline carbon groups ($\text{C}-\text{C/C-H}$), while the peak at $\sim 285.6\text{ eV}$ is associated with alcohol groups (C-OH), and the peak at $\sim 286.8\text{ eV}$ corresponds to ether groups (C=O). The deconvoluted O1s spectrum showed the presence of three peaks at ~ 531 , ~ 532.5 , and $\sim 534.2\text{ eV}$ ascribed to C=O , C-O , and O-C=O , respectively (Figure 1d).

Surface morphology and internal structure of the RG sample were studied with the help of field emission-scanning electron microscopy (FE-SEM) and transmission electron microscopy (TEM). The FE-SEM images of the RG (Figure 2a–d) represent flaky morphology with similar surface features as that of natural graphite material. The TEM image of the sample (Figure 2e) displays clear lattice fringes indicating the layered structure (graphene layers) of RG material. The TEM image also illustrates the purity of RG material, representing the complete removal of decomposition products during the recycling process. The selected area electron diffraction (SAED) measurements confirm the formation of the honeycomb-like structure, which is none other than the formation of the ordered hexagonal graphitic structure with triangular geometry (Figure 2f). In addition, the elemental mapping studies are performed to ensure the distribution of the individual elements. Apparently, very dense mapping is observed for the case of carbon compared to the fluorine, and oxygen indicates its dominance. (Figure 2g–j). This result has been clearly validated from the XPS studies, in which the composition of elements like carbon (91.7 at. %) and oxygen (8 at. %), traces of F (0.3 at. %) were present in the sample. But the amount of

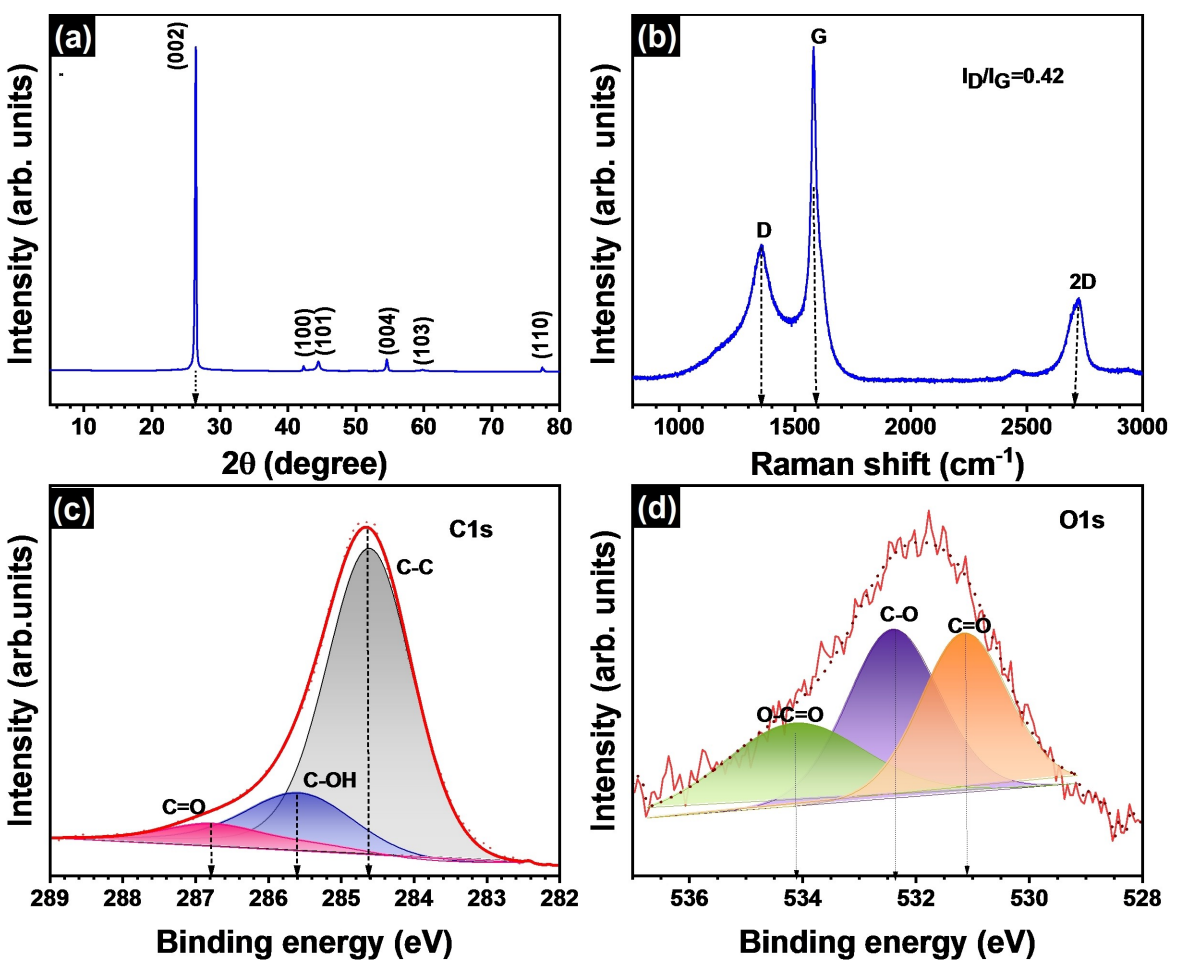


Figure 1. Powder properties of RG: a) powder-XRD pattern, b) Raman spectrum, and c-d) XPS spectra: c) C1s scan and d) O1s scan of RG.

Fluorine is negligibly small in comparison with carbon and oxygen.

To study the co-intercalation of solvated Li-ions into RG, coin half-cells were fabricated with Li metal as a counter electrode in the presence of 1 M LiPF₆ in TEGDME as the electrolyte. The TEGDME is a polar aprotic solvent that enables a high solubility of the Li-salt (LiPF₆) to produce a highly-conducting solution with excellent chemical and thermal stability. Usage of TEGDME (G₄), ether-based electrolyte, enables the co-intercalation of solvated Li-ions into RG at different potentials than that of conventional intercalation representing the formation of LiC₆. The assembled Li/RG half-cells exhibited an open circuit potential (OCV) of ~3.3 V vs. Li, and the cells were tested within the voltage window of 0.05–2.00 V vs. Li. The cell reaction for the Li/RG half-cell can be represented with the following equations [Eqs. (1), (2)]



Where $[\text{Li} - \text{G}_4]^+$ represents the solvated Li-ion, $[\text{Li} - \text{G}_4]\text{RG}$ represents the recovered graphite Li intercalation compound, which is a ternary graphite intercalation compound (t-GIC).

Figure 3a illustrates the cyclic voltammetry (CV) profiles of the first four cycles of the Li/RG half-cell recorded at a scan rate of 0.1 mV s⁻¹. Reversible reduction (~0.75, and ~0.26 V vs. Li) and oxidation (~0.42, ~1.05, and ~1.42 V vs. Li) peaks could be ascribed to solvated Li-ion intercalation and deintercalation into/from RG material. The prominent cathodic peak at ~0.75 V vs. Li in the first cycle, the magnitude tends to decrease upon further cycling, represents the formation of the robust SEI layer by the decomposition of the electrolyte. However, the observed co-intercalation redox potential ~0.75 V vs. Li for the graphitic anode is much higher than the ~0.15 V vs. Li for the typical intercalation phenomenon. Moreover, irrespective of alkali ion species (Li, Na, and K), similar charge-discharge profiles and intercalation potentials corresponding to slope and position of voltage plateau during the co-intercalation process involves the common reaction mechanism. Whereas, it was reported that the average voltage of the graphite electrode increases with the size of the ion such that Li < Na < K. Thus, in comparison with Li insertion, Na or K insertion into graphitic material is energetically more favorable when the ionization

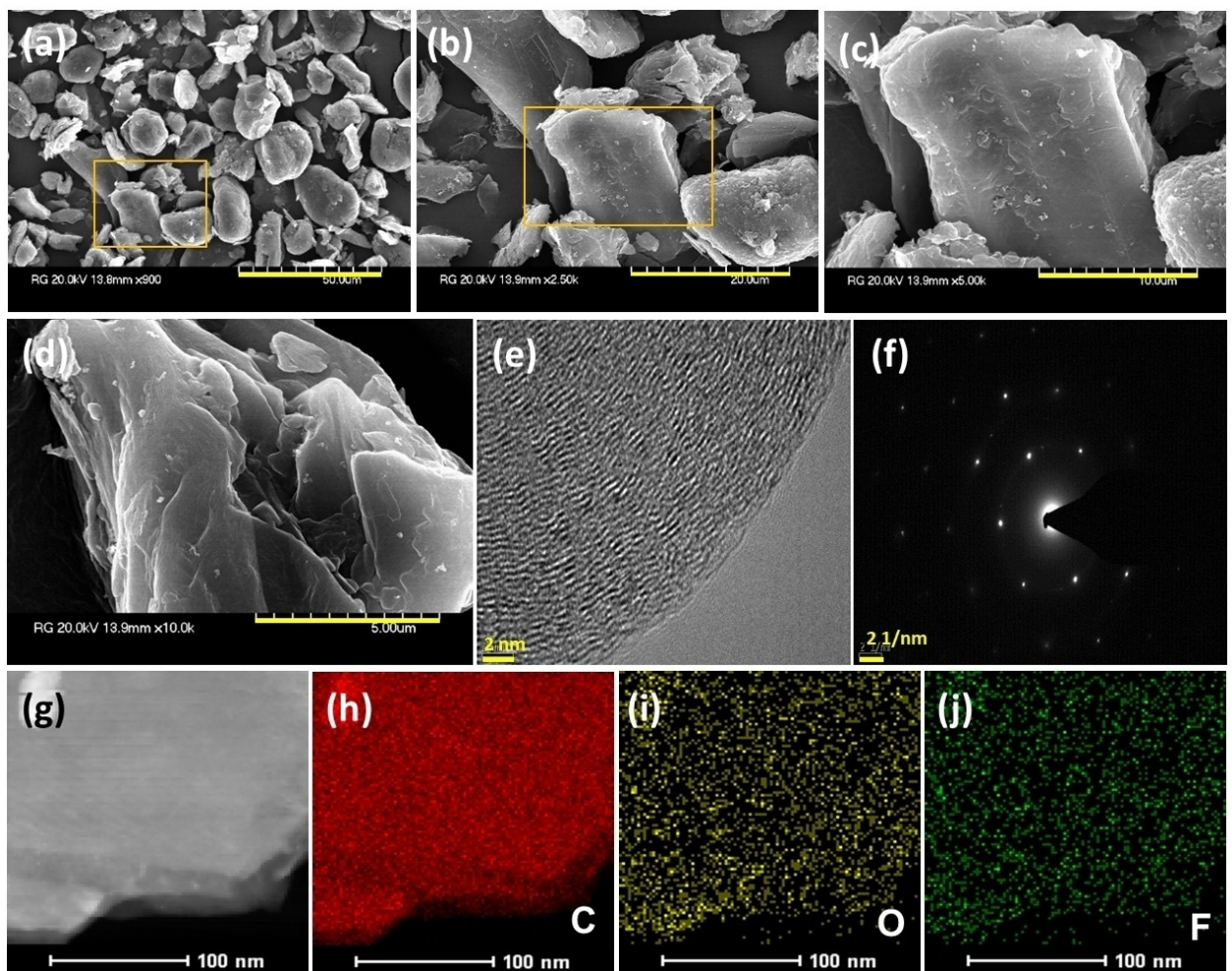


Figure 2. Morphological features of RG: a–d) FE-SEM image at different magnifications, e) HR-TEM image, f) SAED pattern, and g–j) elemental mapping pictures of RG.

energy is not considered. The best evidence for the co-intercalation mechanism is the change in intercalation potential in comparison with conventional intercalation potential. Kim *et al.*^[33] suggested that co-intercalation occurs through staging phenomena, such that the intercalants occupy every n^{th} layer, leaving the interlayers empty. Figure S3 represents the CV profile at different scan rates ranging from 0.1 to 1 mVs⁻¹. It is clear from the profile that, increase in scan rate cause an increase in separation between reduction and oxidation peaks, which corresponds to higher polarization. At the same time, the well-distinguished peaks at all scan rates indicate the presence of very fast redox kinetics in the LiPF₆ -TEGDME system. Figure 3b displays the Randles-Sevcik plot of peak current vs. square root of scan rate. The anodic and cathodic diffusion coefficient of solvated Li-ions is obtained as 4.8×10^{-4} cm²s⁻¹ and 6.2×10^{-4} cm²s⁻¹, respectively. However, the obtained values are higher than the reported value of 10^{-6} cm²s⁻¹, corresponding to bare lithium ion diffusivity in the direction parallel to the graphene plane.^[34] Figure 3c displays the charge-discharge profile of RG in half-cell assembly at the current density 0.1 A g⁻¹ within the potential window of 0.05 to 2.0 V vs. Li. The cell delivered a first discharge capacity of

~ 234 mAh g⁻¹ with initial Coulombic efficiency (ICE) of $\sim 38\%$. This low ICE indicates the formation of an SEI layer during the first cycle. For the second cycle, the cell showed a discharge capacity of ~ 112 mAh g⁻¹ with an efficiency of 78%. This tendency of improved CE value from the second cycle onwards indicates the formation of a stable and robust SEI layer. Figure 3d displays the stability of the cell for the initial twenty cycles. At the twentieth cycle, the cell exhibited a discharge and charge capacity of ~ 90 and ~ 73 mAh g⁻¹, respectively, with an efficiency of 81%. The observed cycling profiles are consistent with the previous report by Kim *et al.*^[33] The study shows that the nature of the SEI layer on Li metal in contact with glyme-based electrolyte is different from that observed in Na-based systems. It was reported previously that the SEI on Li metal electrodes in contact with glyme-based electrolytes nurtures even under open-circuit conditions, pointing that its resistance (R) is proportional to the thickness of the SEI layer. The growth rate of the SEI layer on the surface of Li metal in the presence of glyme-based electrolyte specifies the parallel growth of interfacial and diffusion dominated phases.^[35] Bieker *et al.*^[36] also pointed out that TEGDME based electrolytes are not suitable for Li metal anodes at reasonable current densities

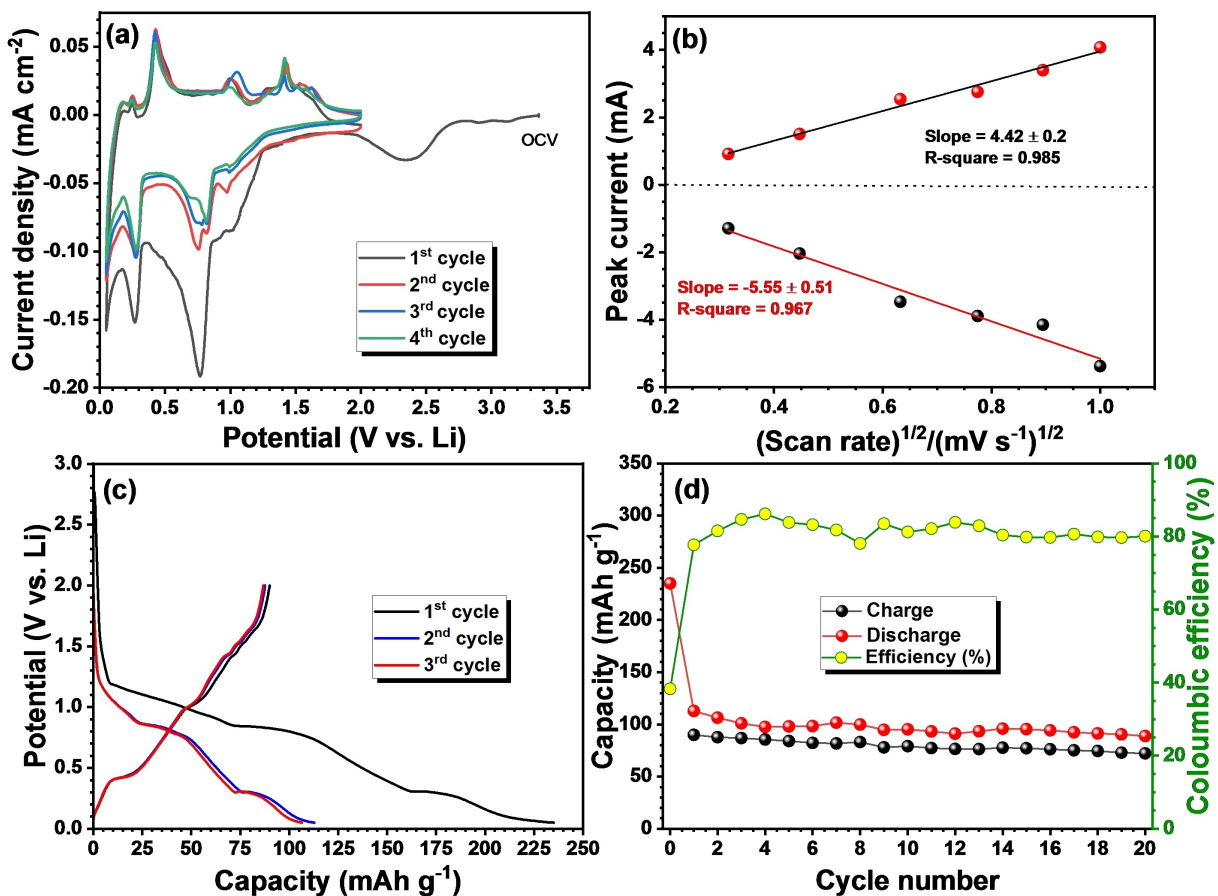


Figure 3. Electrochemical performance of Li/RG half-cell: a) CV curves at 0.1 mVs^{-1} , b) Randles -Sevcik plot of peak current vs. square root of scan rate in 1 M LiPF_6 in TEGDME (red sphere line is experimental oxidation plot and black sphere line is reduction plot), c) typical charge-discharge curves at a current density of 0.1 A g^{-1} , and d) plot of specific capacity vs. cycle number.

due to dendrite formation and electrolyte decomposition and hence SEI layer formation on Li metal. Besides, it was also observed that the cell exhibits poor rate performance with maximum specific capacity at an input current rate of 0.1 A g^{-1} ; due to irreversible damage of the electrode at higher current rates, the capacity values do not recover.^[37] In contrast, Na-based systems exhibit good rate performance such that irreversible damage of electrode is not happening.^[33]

To validate the feasibility of using an AC electrode as a cathode in LIC assembly, Li/AC half-cells were assembled with the same electrolyte solutions. The cells displayed an OCV of $\sim 3.4 \text{ V}$ vs. Li. The galvanostatic charge-discharge study shows a linear charge-discharge profile with an initial discharge capacity of $\sim 74 \text{ mAh g}^{-1}$ at a current density of 0.1 A g^{-1} (Figure S4) for balancing the active mass loading.^[35–36] The linear charge-discharge profile indicates the capacitive storage of the AC electrode. Figure S5 illustrates the electrochemical impedance spectra (EIS) for both the half-cells. The Nyquist plot was considered in the frequency range of 10 kHz to 1 Hz with an applied amplitude of 10 mV . For Li/RG half-cell, the Nyquist plot consists of a semicircle from high to medium frequency range with low-frequency line steeper than 45° corresponds to Warburg type impedance representing the phenomenon of solvated Li-ion diffusion. For Li/AC, half-cell Nyquist plot

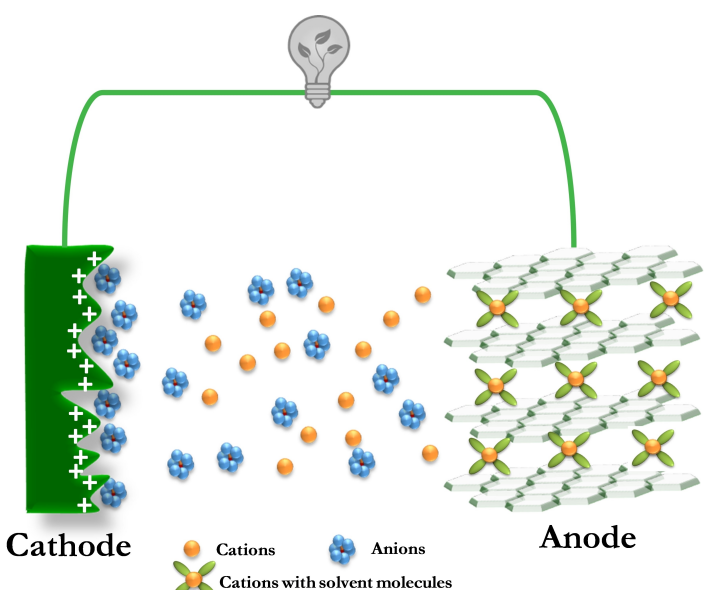
consists of a semicircle with comparatively less diameter in the high to medium frequency range with a short tail in the low-frequency region. The semicircle in the high to medium frequency region indicates the solution resistance and charge-transfer resistance on the electrode surface.

Even though the half-cells are showing less cyclic stability and lower coulombic efficiency, the performance of the electrodes with the same electrolyte system was considered for LIC assembly due to the absence of metallic Li electrode. Also, the choice of potential window for LIC operation is less than that of cathode half-cell. The LIC was assembled by using a p-RG electrode as an anode and an AC electrode as the cathode. The pre-lithiation was done in half-cell assembly by fabricating a Li/RG half-cell and was subjected to two complete discharge charge cycles, followed by a third discharge up to 0.05 V vs. Li. The cell was disassembled in the discharged state, and the lithiated RG electrode (p-RG) was paired with an AC electrode of balanced mass. Mass balancing of the electrodes was done by considering the second discharge capacity of Li/RG half-cell ($\sim 112 \text{ mAh g}^{-1}$) with the initial discharge capacity of Li/AC half-cell ($\sim 74 \text{ mAh g}^{-1}$). And hence, the fabricated LICs exhibited a cathode to anode mass ratio of ~ 1.5 with a total mass of $\sim 5\text{--}6 \text{ mg}$. The thus formed LICs displayed an OCV of $\sim 2 \text{ V}$ and were tested within the potential window of $1.3\text{--}3.8 \text{ V}$ at different

current density ranges from 0.1–3.0 A g⁻¹. The LIC was tested at different current values calculated by considering the total mass of active material in both the electrodes. As LIC has two different electrodes, two different charge storage mechanisms are involved in the charge storage process. As mentioned, the two different charge storage mechanisms involved in LICs like solvent-co-intercalation and physisorption processes are schematically represented in Scheme 1. During charging and discharging, the solvated Li-ions get intercalated and deintercalated into/from RG material, whereas adsorption and desorption of PF₆⁻ takes place on the AC electrode along with the formation of double-layer capacitance. Figure 4a illustrates the CV profile of the LIC at the scan rate of 1 mV s⁻¹ for the first four cycles. Figure 4b clearly shows the difference in CV profile for both the electrodes in half-cell and LIC configuration at a scan rate of 1 mV s⁻¹. Involvement of two different charge storage mechanisms in LIC can be seen in the CV profile with clear distortion of rectangular-shaped CV profile of AC electrode and CV trace with clear oxidation-reduction peaks for RG electrodes. Figure 4c describes the galvanostatic charge-discharge profile for the LIC at different current densities. The near-linear/distorted charge-discharge curves represent the hybrid energy storage mechanism. The cyclic stability of LIC was tested at different current densities like 0.5, 3, and 4 A g⁻¹. The cell exhibited better stability at higher current rates in comparison with low current rates. At 0.5 A g⁻¹, the cell capacity was gradually dropped to ~50% of the initial value after 1000 charge-discharge cycles; and the capacity was completely faded within 4000 cycles, whereas the LIC could exhibit stable performance at higher rates (3 and 4 A g⁻¹) even after 4000 complete charge-discharge cycles Figure 4d. This study clearly illustrates that this kind of solvent-co-intercalation based intercalation phenomena in battery type electrodes (e.g., graphite) are well suited for the high power applications compared to the conventional carbonate-based electrolytes.^[15]

The absence of metallic Li translates to better stability, which is clearly seen from the cycling profiles of AC/p-RG. The energy and power density values of assembled LIC were calculated using standard equations by considering the total mass of active material in both the electrodes. The assembled dual carbon LIC with glyme-based electrolyte system could deliver a maximum energy density of 46.40 Wh kg⁻¹ with a power density of 248 W kg⁻¹ when a current density of 0.1 A g⁻¹ was applied at ambient conditions. Moreover, the cell also exhibits a capacity to give a maximum power of 5.64 kW kg⁻¹ with an energy density of 8.84 Wh kg⁻¹ when the current applied rate is switched to 3 A g⁻¹. In addition, the performance of LIC was also tested at various temperature conditions to check the compatibility of the cell at different environmental conditions. Figure 4e illustrates the Ragone plot of fabricated LIC at different temperature conditions (50, 25, 10, and -5 °C). The LIC could deliver a maximum energy density of 52.37, 30.20, and 18.01 Wh kg⁻¹ with a power density of ~248 W kg⁻¹ at a current density of 0.1 A g⁻¹ for the temperatures 50, 10, and -5 °C, respectively. Figure 4f shows the galvanostatic charge-discharge profiles at the current density of 0.1 A g⁻¹ for various temperature conditions. The poor performance of LIC at low-temperature conditions can be explained by the reasons for increased cell polarization due to sluggish kinetics of solvated Li-ions. Figure 4g displays the comparison of the Nyquist plot of LIC operated at different temperature conditions. Increased solution resistance and charge-transfer resistance at low-temperature conditions clearly explain the poor low-temperature performance of LIC.

Further, we made a comparison of performances for the dual carbon glyme-based LIC (AC/p-RG) in this study with previously reported dual carbon LIC (AC/p-RG) with conventional carbonate-based electrolytes. Figure S6 illustrates the Ragone plot with energy and power density values of both the LICs at various current rates for 25 and 50 °C. It is very clear that



Scheme 1. Schematic representation of the LIC based on the two-different charge-storage mechanisms.

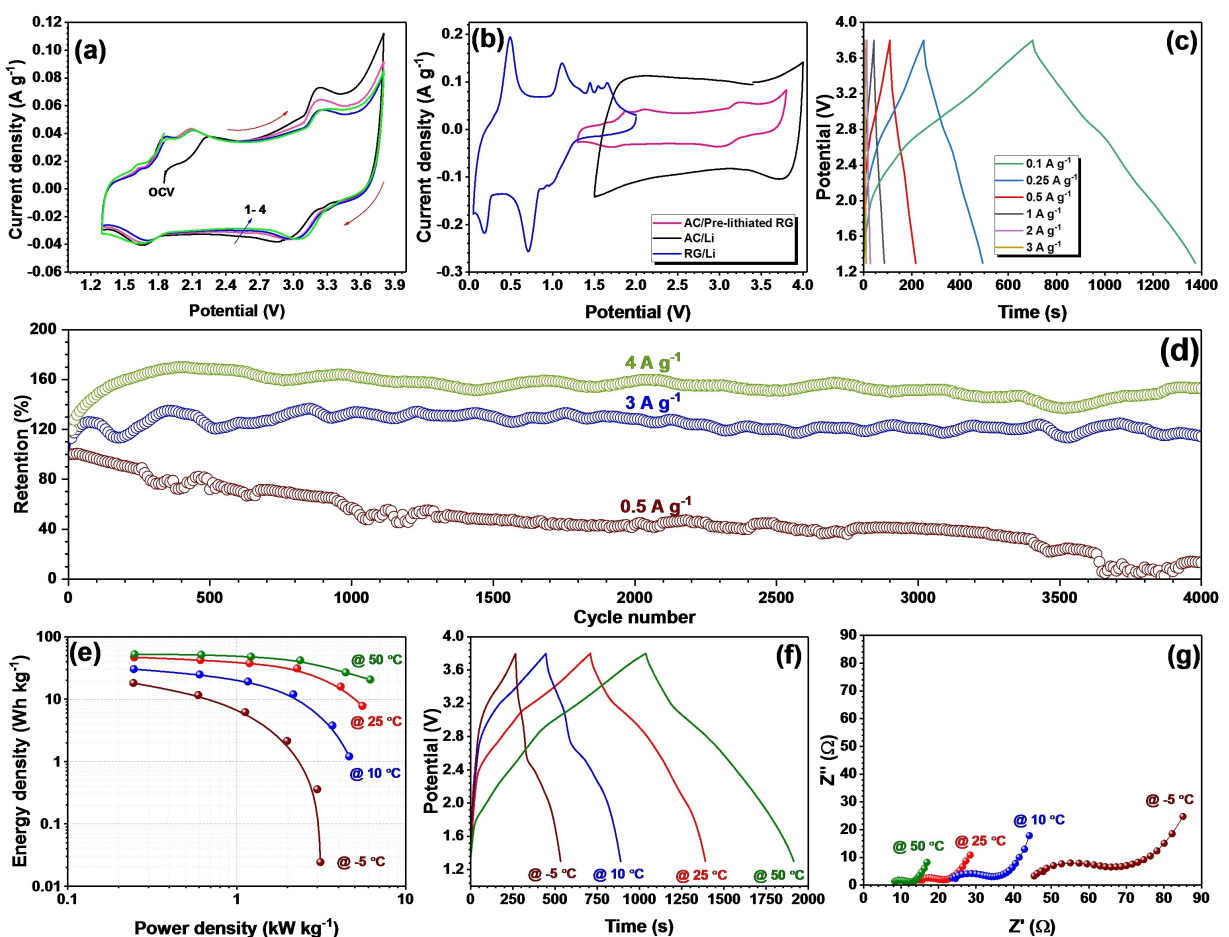


Figure 4. Electrochemical performance of AC/RG based LIC: a) CV curves at the scan rate of 1 mV s^{-1} , b) comparison of the CV curves of RG and AC in half-cells and LIC configuration at the scan rate of 1 mV s^{-1} in 1 M LiPF_6 -TEGDME, c) galvanostatic charge-discharge profile with triangular shape from 0.1 to 3 A g^{-1} , d) long-term cyclability of LIC at different current densities, e) Ragone plot at different temperature conditions, f) galvanostatic charge-discharge profile at the current density of 0.1 A g^{-1} for different temperature conditions, and g) Nyquist plot of fabricated LIC at different temperature conditions.

LIC with glyme-based electrolyte is showing inferior performance in comparison with conventional carbonate-based electrolyte system in terms of the quantity of energy it can store whereas, the cyclability of the cell at high current rates is dominating. The values are not at all comparable to the conventional carbonate-based solution, which is mainly associated with the lower Li-intercalation potential ($\sim 0.15 \text{ V}$ vs. Li). However, the lower intercalation potential often leads to Li-plating in the presence of flammable solutions. Further, the discharge product LiC_6 is one of the strong reducing agents. In the case of glyme-based solutions, such kind of plating issue is averted due to higher intercalation potential with non-flammable electrolyte. As mentioned, the direct interaction with solvated Li-ion and the graphene layers are unfavorable, and hence the formation of the LiC_6 is minimized with the presence of a solvent shell. Further research activities are essential to improve the energy density of the LICs since this is the first report on the electrochemical activity of Li-based glyme solutions in the hybrid configuration.

3. Conclusion

In this study, we successfully demonstrated the fabrication of a new kind of dual carbon LIC, with glyme-based electrolyte (1 M LiPF_6 in TEGDME) using recovered graphite from the spent LIB as anode and commercial AC as a cathode. Before the LIC assembly, the RG was electrochemically pre-lithiated. The assembly AC/RG delivered a maximum energy density of $\sim 46.40 \text{ Wh kg}^{-1}$ at room temperature. However, in terms of cyclability and safety, the glyme-based LIC could dominate the conventional carbonate-based electrolyte solutions. However, it was observed that half-cell performance of both the electrodes exhibited less stability in combination with glyme and Li anode, which can be explained by the fact that the nature of SEI layer on Li-metal in contact with glyme-based systems is completely different from that observed for Na-based systems. In addition, instability of TEGDME (in Li) solution at high potential can also be considered as one of the reasons for the poor performance of cathode half-cell. However, there are no such issues observed in the LIC assembly. Therefore, the LIC system can be considered a suitable option for low energy and long-term applications. In addition, this study also foresees the applic-

ability of RG from spent LIB for the fabrication of high-performance, low-cost energy storage devices considering the waste-to-wealth approach.

Experimental Section

Recovery of graphite material from spent LIBs

Irrespective of manufactures, mobile phone spent LIBs were collected and kept for complete discharge in NaCl solution for 24 hours to avoid any risk during battery dismantling. The anode part, Cu-foil containing graphite paste, was separated, and the removal of graphite material was performed by a simple sonication procedure using water as the solvent. De-ionized water was used to separate the traces of Li-ions, which could be present on the anode side due to SEI layer formation during the charge-discharge process. Further, centrifugation with dimethylformamide (DMF) ensured the complete removal of graphite. The graphite was collected and washed with distilled water and kept in a hot air oven for complete drying. The material was heat-treated at 700 °C for 2 hours in the Ar atmosphere before using it as the active electrode material for cell fabrication.

Physiochemical characterization

The recovered graphite material (RG) was characterized using various analytical techniques like Power X-ray diffraction (XRD, Rigaku, Smartlab 9 kW, Japan) with Cu K α radiation, Raman spectroscopy (LabRam HR800 UV Raman microscope, Horiba Jobin-Yvon, France), X-ray photoelectron spectroscopy (XPS with a Multilab instrument (monochromatic Al K α radiation $h\nu = 1486.6$ eV), field emission scanning electron microscopy (FE-SEM, S-4700, Hitachi, Japan), and High-resolution transmission electron microscopy (HR-TEM, HR-TEM, TECNAI, Philips, the Netherlands, 200 keV). And an energy dispersive spectrometer attached to the HR-TEM was used for energy-dispersive X-ray spectroscopy (EDS) mapping.

Electrode preparation and cell assembly

The recovered graphite (RG) electrode was formulated by mixing the active material (RG), conductive carbon (acetylene black), and polyvinylidene fluoride binder in an 80:10:10 ratio using N-methyl pyrrolidone as the solvent. The slurry was stirred to get uniform mixing for a minimum period of 6 hours, and then it was coated on the Cu-foil with the doctor blade technique. The foil was dried overnight within the hot air oven and pressed under a hot roll press machine (Tester Sangyo, Japan). Disc electrodes of 14 mm diameter were cut out from Cu-foil using an electrode cutter. Likewise, activated carbon (AC, YP 80F Surface area: $2100\text{ m}^2\text{ g}^{-1}$, Pore volume: 0.97 ml g^{-1} , Kuraray, Japan) electrode material was also made by mixing AC, conductive carbon (acetylene black), and binder (teflonized acetylene black, TAB-2) with the ratio of 80:10:10 using ethanol and pressed on a 16 mm diameter stainless steel mesh (Goodfellow, UK) that served as the current collector. Both the electrodes were dried within a vacuum chamber at 75 °C for a minimum of 4 hours before cell fabrication. The electrochemical performance of RG and AC were tested in half-cell assembly (CR 2016) with Li metal. The cell fabrication was done within an Ar-filled glove box using 1 M LiPF₆ (Sigma-Aldrich) in TEGDME (Sigma-Aldrich) as electrolyte and Whatman paper (1825-047, GF/F) as a separator. Prior to the fabrication of LIC, the RG was

electrochemically pre-lithiated, which serves as an anode and an AC electrode with balanced mass loading conditions.

Electrochemical characterization of half-cells and LIC

The electrochemical testing for the assembled half-cells (Li/RG and Li/AC) and LICs (AC/RG) were performed with a battery tester (Biologic, France). The electrochemical impedance spectroscopy (EIS), galvanostatic charge-discharge studies, and cyclic voltammograms were recorded for both half-cell and LIC configurations using the above-said battery tester. The half-cell studies were done not only to validate the suitability of these electrodes with 1 M LiPF₆ in the TEGDME electrolyte towards the fabrication of LIC but also to adjust the mass loading between the active materials like RG and AC. The pre-lithiation was done with half-cell assembly by discharging the cell to 0.05 V vs. Li at a current density of 0.1 A g^{-1} followed by two complete discharge-charge cycles. The RG electrode in the lithiated phase was separated carefully with a de-crimper and used for LIC assembly. The electrochemical testing of AC/RG-based LIC was tested at different current rates ($0.1 - 3\text{ A g}^{-1}$) within the potential window of 1.3–3.8 V. The energy and power density of fabricated LICs were analyzed based on the total mass of active material present in both the electrodes. The performance of assembled LIC was also tested at different temperature conditions using an environmental chamber (Espec, Japan).

Acknowledgments

M.L.D. wishes to thank the funding through Women Scientist Scheme-B (DST/WOS-B/2018/2039) from the KIRAN division of the Department of Science & Technology (DST), Govt. of India. V.A. acknowledges financial support from the DST through Swarna-jayanti Fellowship (DST/SJF/PSA-02/2019-20) and Grant by Science and Engineering Research Board (SB/SJF/2020-21/12). Y.S.L. acknowledges the financial support from the National Research Foundation of Korea (NRF) grant funded by the Korean government (Ministry of Science, ICT & Future Planning) (No. 2019R1A4A2001527).

Conflict of Interest

The authors declare no conflict of interest.

Keywords: Li-ion capacitor • graphite • solvent-co-intercalation • spent Li-ion battery recycling

- [1] <https://www.smart-energy.com/industry-sectors/storage/energy-storage-systems-market-to-expand-by-over-6-per annum/>, in *Smart energy International*, 2020.
- [2] V. Aravindan, J. Gnanaraj, Y.-S. Lee, S. Madhavi, *Chem. Rev.* **2014**, *114*, 11619–11635.
- [3] J. Ding, W. Hu, E. Paek, D. Mitlin, *Chem. Rev.* **2018**, *118*, 6457–6498.
- [4] H. Wang, C. Zhu, D. Chao, Q. Yan, H. J. Fan, *Adv. Mater.* **2017**, *29*, 1702093.
- [5] B. Li, J. Zheng, H. Zhang, L. Jin, D. Yang, H. Lv, C. Shen, A. Shellikeri, Y. Zheng, R. Gong, *Adv. Mater.* **2018**, *30*, 1705670.
- [6] S. Natarajan, Y.-S. Lee, V. Aravindan, *Chem. Asian J.* **2019**, *14*, 936–951.
- [7] V. Aravindan, M. Ulaganathan, S. Madhavi, *J. Mater. Chem. A* **2016**, *4*, 7538–7548.
- [8] V. Aravindan, Y.-S. Lee, *J. Phys. Chem. Lett.* **2018**, *9*, 3946–3958.

- [9] L. Zhang, D. P. Wilkinson, Z. Chen, J. Zhang, *Lithium-ion supercapacitors: Fundamentals and energy applications*, CRC Press, 2018
- [10] R. P. Deshpande, *Ultracapacitors: Future of Energy Storage*, McGraw-Hill Education, 2014.
- [11] S. Trasatti, P. Kurzweil, *Platinum Met. Rev.* **1994**, *38*, 46–56.
- [12] G. Li, Z. Yang, Z. Yin, H. Guo, Z. Wang, G. Yan, Y. Liu, L. Li, J. Wang, *J. Mater. Chem. A* **2019**, *7*, 15541–15563.
- [13] S. S. Zhang, *Batteries & Supercaps* **2020**, *3*, 1137–1146; *Supercaps* **2020**, *3*, 1137–1146.
- [14] T. Panja, J. Ajuria, N. Díez, D. Bhattacharjya, E. Goikolea, D. Carriazo, *Sci. Rep.* **2020**, *10*, 1–11.
- [15] M. L. Divya, S. Natarajan, Y.-S. Lee, V. Aravindan, *J. Mater. Chem. A* **2020**, *8*, 4950–4959.
- [16] P. Sennu, N. Arun, S. Madhavi, V. Aravindan, Y.-S. Lee, *J. Power Sources* **2019**, *414*, 96–102.
- [17] G. Madabattula, B. Wu, M. Marinescu, G. Offer, *J. Electrochem. Soc.* **2019**, *167*, 013527.
- [18] S. R. Sivakkumar, A. G. Pandolfo, *Electrochim. Acta* **2012**, *65*, 280–287.
- [19] V. A. Agubra, J. W. Fergus, *J. Power Sources* **2014**, *268*, 153–162.
- [20] Q. Liu, S. Li, S. Wang, X. Zhang, S. Zhou, Y. Bai, J. Zheng, X. Lu, *J. Phys. Chem. Lett.* **2018**, *9*, 5567–5573.
- [21] T. Ohzuku, Y. Iwakoshi, K. Sawai, *J. Electrochem. Soc.* **1993**, *140*, 2490.
- [22] <https://www.marketwatch.com/press-release/lithium-ion-capacitor-market-2020-top-countries-data-with-future-scope-market-size-definition-opportunities-with-strategic-growth-and-top-key-players-analysis-and-forecasts-to-2026-2020-11-25>.
- [23] S. Natarajan, V. Aravindan, *Adv. Energy Mater.* **2020**, *10*, 2002238.
- [24] C. Yi, Y. Yang, T. Zhang, X. Wu, W. Sun, L. Yi, *J. Cleaner Prod.* **2020**, *277*, 123585.
- [25] S. Natarajan, D. S. Lakshmi, H. C. Bajaj, D. N. Srivastava, *J. Environ. Chem. Eng.* **2015**, *3*, 2538–2545.
- [26] M. L. Divya, S. Natarajan, Y. S. Lee, V. Aravindan, *Small* **2020**, *16*, 2002624.
- [27] K. Subramanyan, S. Natarajan, Y.-S. Lee, V. Aravindan, *Chem. Eng. J.* **2020**, *397*, 125472.
- [28] M. L. Divya, S. Natarajan, Y. S. Lee, V. Aravindan, *ChemSusChem* **2020**, *13*, 5654–5663.
- [29] S. Natarajan, H. C. Bajaj, V. Aravindan, *J. Mater. Chem. A* **2019**, *7*, 3244–3252.
- [30] T. Abe, H. Fukuda, Y. Iriyama, Z. Ogumi, *J. Electrochem. Soc.* **2004**, *151*, A1120.
- [31] J. Park, Z.-L. Xu, K. Kang, *Front. Chem.* **2020**, *8*, 432.
- [32] Y. Li, Y. Lu, P. Adelhelm, M.-M. Titirici, Y.-S. Hu, *Chem. Soc. Rev.* **2019**, *48*, 4655–4687.
- [33] H. Kim, G. Yoon, K. Lim, K. Kang, *Chem. Commun.* **2016**, *52*, 12618–12621.
- [34] K. Persson, V. A. Sethuraman, L. J. Hardwick, Y. Hinuma, Y. S. Meng, A. van der Ven, V. Srinivasan, R. Kostecki, G. Ceder, *J. Phys. Chem. Lett.* **2010**, *1*, 1176–1180.
- [35] M. Nojabaei, K. Küster, U. Starke, J. Popovic, J. Maier, *Small* **2020**, *16*, 2000756.
- [36] G. Bieker, M. Winter, P. Bieker, *Phys. Chem. Chem. Phys.* **2015**, *17*, 8670–8679.
- [37] P. M. Attia, *Degradation of Carbon Negative Electrodes in Lithium-Ion Batteries*, Stanford University, 2019.

Manuscript received: December 10, 2020

Revised manuscript received: December 23, 2020

Accepted manuscript online: December 23, 2020

Version of record online: January 7, 2021